Influence of the scanning strategy on the microstructure and the tribological behavior of a Ni-based superalloy processed by L-PBF additive manufacturing

Pierre-Nicolas Parent, Jean-yves Paris, Joel Alexis, Christine Boher

Wear 564–565 (2025) 205671

Contents lists available at ScienceDirect

Wear

journal homepage: www.elsevier.com/locate/wear

Influence of the scanning strategy on the microstructure and the tribological behavior of a Ni-based superalloy processed by L-PBF additive manufacturing

Pierre-Nicolas Parent [a,b,*], Jean-Yves Paris [b], Joël Alexis [b], Christine Boher [a]

[a] Institut Clément-Ader (ICA); Université de Toulouse; CNRS, IMT Mines Albi, INSA, ISAE–SUPAERO, UPS, Campus Jarlard, 81013, Albi, France
[b] Laboratoire Génie de Production (LGP), UTTOP, Université de Toulouse, 47 avenue d'Azereix, 65000, Tarbes, France

ARTICLE INFO

Keywords:
LPBF-processed ABD-900AM
Wear
Microstructure
Wear track analysis

ABSTRACT

The ABD-900AM is a newly developed nickel-based alloy specifically designed for additive manufacturing, and it can be printed using a wide range of process parameters. This alloy, combined with the L-PBF process, allows for the production of dense parts with reference microstructures that are multi-scale, and facilitates the study of the links between these microstructures and their tribological behaviors. To study the relationships between microstructures and tribological behaviors, the parts are built vertically without interlayer rotation. The plane studied are obtained with three scanning directions : 0°, 45° and 90°. These angles allow to generate different microstructures on the planes on which are conducted the microstructural characterizations and tribological tests, for which the sliding direction is always parallel to the building direction. This choice of parameter enables access to different crystallographic textures (200) and (111), and cellular structures with varying morphologies and homogeneity within the melt pools. Tribological tests were performed on these microstructures in a ball-on-flat configuration with alternating motion, without lubrication, and at room temperature. For the three laser angles (0°, 45°, and 90°), the wear volumes are 0.60 ± 0.12 mm^3, 0.81 ± 0.15 mm^3, and 1.00 ± 0.09 mm^3, respectively. The wear resistance is primarily related to the amount of oxide layers formed on the wear track of the samples.

1. Introduction

Ni-based superalloys, widely used in high-performance applications like aerospace [1,2], are known to withstand high temperatures and offer robust mechanical and corrosion resistance [3]. This robustness, however, also presents significant challenges in their machining due to heat generation, material plasticity, strain hardening, and the presence of abrasive carbides in the microstructure. These factors complicate the machining process and reduce tool life [4]. The emergence of additive manufacturing (AM) processes in the 2000s has sparked interest in academia and industry, as they enable the production of components with complex geometries and offer a potential solution to these challenges [5].

Nevertheless, the Ni-based alloys belonging to the γ/γ' family, such as Inconel 738, are generally considered challenging to weld due to their high (Ti+Al) content [6]. Laser powder bed fusion (L-PBF) is a process whereby successive melt pools are welded together. As a result, applying alloys to L-PBF presents many challenges, with much research focusing on the production of defect-free parts [7–9]. The ABD900AM® belongs to the same alloy family, but its digital development was carried out using the Alloys-By-Design (ABD) method. The development of this alloy has been driven by the pursuit of enhanced processability while maintaining the mechanical properties characteristic of other alloys, such as CM247LC and Inconel 939 [10–12]. The parts undergo many phase transformations during printing, encompassing liquid/solid and solid/liquid states at elevated cooling rates. These transformations will influence the microstructure and generate complexities specific to this process [13,14]. The microstructure is well-established to comprise a cellular structure and grains exhibiting epitaxial growth [15,16]. Recent studies have demonstrated the relationship between process parameters, including laser power and building strategy, and the resulting microstructure and mechanical properties [17–20]. It also reflects the ability to tailor the crystallographic texture with process parameters. In 2021, Sanchez [5] reviewed the mechanical properties of Powder Bed Fusion (PBF) nickel-based superalloys, but the tribological properties were not discussed, indicating a need for further research. The studies covering the tribological properties of Ni-based superalloys made by laser powder bed fusion (L-PBF) have been published mainly since 2020

* Corresponding author at: Institut Clément-Ader (ICA); Université de Toulouse; CNRS, IMT Mines Albi, INSA, ISAE–SUPAERO, UPS, Campus Jarlard, 81013, Albi, France.
E-mail address: pierrenicolas.parent@uttop.fr (P.-N. Parent).

https://doi.org/10.1016/j.wear.2024.205671
Received 26 September 2024; Received in revised form 22 November 2024; Accepted 24 November 2024
Available online 3 December 2024

Table 1
Chemical composition of the powder at as-received state.

Elements	Ni	Cr	Co	Mo	W	Al	Ti	Ta	Nb	C	B	Zr	O	N
wt%	49.8	17.0	20.4	2.1	3.1	2.1	2.3	1.5	1.8	0.049	0.004	<0.01	0.011	0.010

Table 2
Building parameters.

Laser power	Laser speed	Hatching distance	Layer thickness	Interlayer time
275 W	760 mm/s	120 μm	50 μm	63 s

and have gathered more than 20 articles. Previous studies have primarily concentrated on the process parameters and post-treatments and have established a correlation between these factors, the resulting tribological and hardness properties, and the microstructure. Liu et al. [21] and Jia et al. [22] studied how the laser parameters affected cells and porosity and exhibited that increased porosity implies a decrease in hardness and wear performance. The influence of scanning strategy on microstructure and tribological properties has only been investigated by Yan et al. [23]. The parts were printed following three building directions (0°, 45° or 90°) and with an interlayer rotation of 67°, which is well known to be almost untextured from a crystallographic point of view. The results show a correlation between the building direction of the parts and the resulting wear rates. Other researchers worked on building strategies for 316L [24,25] and found slight differences linked to the normal load and the scanning strategy used. For example, Bahshwan et al. [25] related the good wear performance with the number of high-angle grain boundary intersections on the friction surface with the Hertzian contact and the resulting work-hardening rate.

In summary, the influence of scanning strategy on the microstructure and its tribological properties for Ni-based superalloys made by L-PBF has yet to be covered in the literature. This study has two main objectives. The first one is to assess the relationships between the scanning strategy and the microstructure. With the additive manufacturing process, changes of morphological and crystallographic textures. And the second one is to understand the relationships between those microstructures and the corresponding tribological behavior. The resulting microstructure is characterized by an X-ray diffractometer (XRD) and a range of observation techniques. Wear characterization is based on the wear volume, and the wear track, wear particles, and the wear surface cross-section are further analyzed with a scanning electron microscope (SEM) equipped with an energy dispersive spectroscopy (EDS) and backscattered electron (BSE) detector.

2. Materials and method

2.1. ABD-900AM processed by L-PBF

ABD-900AM powder was prepared by Ar-gas atomization. The supplier provides the powder size and chemical composition (Aubert & Duval®). The particle size distribution is D10 = 18.6 μm, D50 = 31.8 μm and D90 = 54.3 μm. The chemical composition is in Table 1.

The L-PBF machine used to build the parts is an SLM 125HL from SLM Solutions. During the fabrication, the steel substrate was preheated to 200 °C to reduce thermal stresses, and an argon protective gas was used to maintain the quantity of oxygen below 0.2%. The samples used in this study are parallelepipeds of $15 * 15 * 5$ mm^3. They are processed with the parameters in Table 2.

The samples were constructed vertically using a bidirectional scanning pattern and without interlayer rotation. The angle between the scanning direction and the tribological studied plane (YZ) is modified to generate different crystallographic and morphological textures. The three angles under consideration are 0°, 45°, and 90°. The samples produced with these angles will be designated AX-Y, with X representing the scanning angle and, if necessary, Y denoting the test number. All characterizations and tests are conducted on the samples in their as-built state. Fig. 1 illustrates the schematic representation of the printed parts following the three scanning strategies.

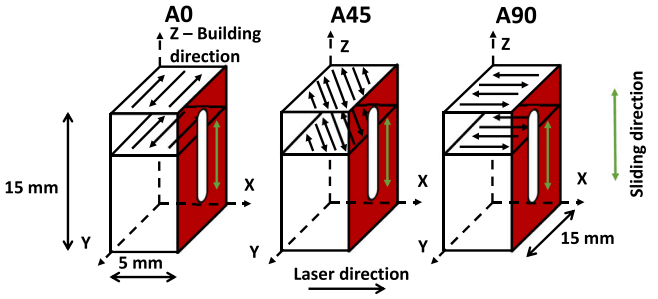

Fig. 1. Schematic representation of the different building strategies. The reference plane for conducting microstructural characterization and tribological tests is in red. (For interpretation of the references to color in this figure legend, the reader is referred to the web version of this article.)

2.2. Microstructural characterizations

Different techniques can determine the relative density of additive manufactured metals. The most common are image analysis, the Archimedes method, and X-ray imaging [26]. Image analysis is used for this study because it allows us to distinguish every type of default, measure their size, and classify them. The relative density was calculated using image analysis with the ImageJ free software. Before image analysis, the samples were polished until OPS (Oxide Polishing Suspension) and observed with an optical microscope. Each result of relative density is based on the measurement of 10 images, each with a size of $0{,}78 \times 0{,}66$ mm^2. With these measurements, we consider every element not part of the based material: porosities, cracks, and phases like aluminum oxides.

For metallographic observations, the samples were mounted, grounded, and then electrolytically etched with 10% oxalic acid at room temperature under 3 V DC for 3 s to 10 s, following the size of the surface to etch. The sections were observed using an optical microscope Olympus PMG3 and SEM from ZEISS EVO HD15LS, equipped with an EDS and a BSE detector, to analyze the macro and microstructures. X-ray diffraction analysis (XRD) was conducted with a Panalytical X'Pert MRD diffractometer equipped with a position-sensitive detector (PSD) with a scan speed of 0,008023°/s over 2θ = 40–100°. The source is a copper radiation (λ = 0,154056 nm, 40 kV and 50 mA) with a capillary collimator of 500 μm and a nickel filter.

2.3. Hardness measurements and tribological tests

Hardness tests were conducted on the studied surfaces (red surface in Fig. 1) of the samples to characterize the different scanning strategies. Hardness was measured using a DuraScan of ZwickRoell with a load of 1 kg (HV_1) and a dwelling time of 10 s. 25 hardness indentations were made to obtain hardness averages and their corresponding standard deviation.

Dry sliding tests were performed at room temperature using a UMT TRIBOLAB of Bruker to study the tribological behavior and were repeated three times for each scanning strategy. A picture of the experimental device with a schematic representation of the friction test is in Fig. 2. The device used is equipped with sensors to measure the normal load (Fz) and the tangential load (Fx) with an acquisition frequency of 200 Hz and the tribometer software calculates the real-time coefficient of friction (COF). Before wear tests, the samples were mounted and mechanically grounded until paper SiC P1000 to

Table 3
Tribological test parameters and Hertz pressure.

Normal load	Frequency	Stroke length	Test duration	Maximal Hertz pressure
30 N	1 Hz	10 mm	3600 s	1.6 GPa

Table 4
Relative density of the parts for the three scanning strategies.

Scanning strategy	Relative density (%)
A0	99,8 ± 0,1
A45	99,8 ± 0,1
A90	99,9 ± 0,1

eliminate the roughness generated by the process, which can reach a primary profile height of up to 220 μm. The roughness after the P1000 surface finishing has been measured with an Altisurf wide-field confocal microscope. The measurements show that the plan has a roughness (R_a) of 0.159 μm before wear tests. On each sample, two tribological tests can be performed. Consequently, two samples were prepared for each laser strategy to conduct three tribological tests per strategy. This last polishing step also removes the edges where a gradient of mechanical properties may exist. The geometrical configuration of the wear tests was a ball-on-flat configuration with an alternating sinusoidal motion. The balls used for tribological tests are in alumina (Al_2O_3) with a 10 mm diameter. The tribological test parameters and Hertz pressure are grouped together in Table 3.

For each test, the sliding direction was parallel to the building direction (Z axis in Fig. 1). Before the wear tests, the sample and the ball were cleaned in ultrasonic baths of acetone and ethanol for 5 min each. To calculate the wear volume (V), the wear surface cross-section was measured with an Altisurf wide-field confocal microscope and then integrated into the length of the wear track (Fig. 2b). An optical microscope Keyence VHX-6000 visualized the antagonists right after the tests, with the particles still present on the counter bodies.

The chosen wear indicator for the ball is the wear volume (V_b). Based on optical micrographs acquired with the Keyence VHX-6000, the calculation of the wear volume involves the dimensions of the 2D projection of the ball's wear track which are also used to calculate the worn height (h_u) of the ball. This calculation relies on two strong assumptions. The first is that the wear track is perfectly flat, and the second is that the wear track is perfectly circular. However, in reality, the wear track exhibits a radius of curvature greater than that of the unworn ball, as previously reported in the literature [27]. Additionally, the radius is not equivalent along the transverse and longitudinal directions relative to the sliding direction. Furthermore, the morphology of the wear track in a reciprocating motion configuration can be either circular or elliptical, as observed in various studies [27–30]. To account for the evolving morphology of the wear track, Whitenton and Blau [30] proposed Eq. (1) to calculate the worn height, which incorporates the minor and major axes of the wear track.

$$h_u = r - \sqrt{r^2 - \frac{L_x * L_y}{4}} \tag{1}$$

Here, r is the radius of the ball, while L_x and L_y represent the minor and major axes of the ball's wear track, respectively. According to the same authors, the wear volume of the ball (V_b) can be determined using Eq. (2):

$$V_b = \frac{\pi * h_u^2 * (3 * r - h_u)}{3} \tag{2}$$

3. Results & discussion

3.1. Microstructure characterizations

The relative density of the as-fabricated samples is investigated for each scanning strategy (Table 4). The relative density is high (>99%) for all the samples meaning that all the samples are almost dense.

To investigate the microstructure, the reference planes were observed with an optical microscope after etching and with an SEM before and after etching (Fig. 3) for each scanning angle.

The observations made with the optical microscope indicate that the shape of the melting pool is dependent on the scanning strategy employed. As the melt pools are aligned with the laser direction, their longitudinal and cross-sectional areas appear in the reference plane of sample A0 and samples A45 and A90, respectively. The fusion baths are asymmetrical for sample A45 due to the angle of the lasering with the reference surface. For the A45 and A90 strategies, the cellular structure is coarser between the melt pools. In this region, the cells are predominantly equiaxed for the Ang45 strategy and columnar for the Ang90 strategy.

The SEM images acquired with the BSE detector before etching demonstrate the presence of distinct grain structures for the three scanning angles. The A0 (Fig. 3d) and A45 (Fig. 3e) strategies display grains exhibiting minimal epitaxial growth, with the A0 grain structure being more refined than that observed in A45. Fig. 3f illustrates that the A90 sample predominantly comprises columnar grains aligned with the building direction. The observations made at higher magnification after etching permit an assessment of the fine microstructure that developed during solidification. The A0 part (Fig. 3g) comprises equiaxed cells, while the A45 part (Fig. 3h) mainly comprises equiaxed cells and some columnar cells. A90 (Fig. 3i) comprises columnar cells and equiaxed cells. These observations show a strong relation between the scanning angle and the macro/microstructure developed, from the cell scale to the melting pool scale.

SEM analysis at high magnification, shown in Fig. 4, was conducted to characterize the phases present in the microstructure. It mainly comprises equiaxed cells and Laves phase in the intercellular regions, resulting from the microsegregation during solidification. The microstructure consists of submicronic circular particles mainly dispersed in the intercellular areas. A recent study on ABD-900AM of Tang et al. [31] shows that these particles are primarily MC-type carbides rich in Ti/Nb/Ta, alumina oxides, borides, and sulfur but in a much lower quantity. They also used STEM-EDS to evaluate the chemical composition of the cell boundaries, and they measured a clear segregation of Ti, Ta, and Nb, showing a slight trend close to the noise level. The three scanning angles have the same phases: cells with Laves phase and submicronic particles in the intercellular regions.

3.2. Phase analysis

XRD measurements have been carried out to understand the preferential texture developed during the L-PBF process. Based on Bragg's law, diffraction peaks correspond to the crystallographic planes parallel to the surface; the texture can be approached if there is one intense peak and the others almost off.

The XRD measurements in Fig. 5 show the diffraction peaks of the γ (Ni-Cr-Co) matrix. It is well known in literature that the matrix has a face-centered cubic (fcc) crystallographic structure [32]. The diffraction peaks of the γ' precipitates with an L12-ordered face-centered cubic (fcc) crystal structure are not detectable at the as-built state in the range observed and are not supposed to be detected. Indeed, other studies showed that γ' is not present in the as-built state for the ABD-900AM [12,31].

The A0 and A90 samples have a strong texture along the γ(200) plane, while A45 has a γ(111) texture. The result of A0 is unusual if we refer to the literature existing on Ni-based superalloys fabricated by L-PBF [33,34]. According to these authors, the texture expected is γ(101). The samples were printed on the same plate with the same laser parameters; the reason for this unusual texture may be attributed to the part geometry, which is rectangle. Scanning vectors of A90 being

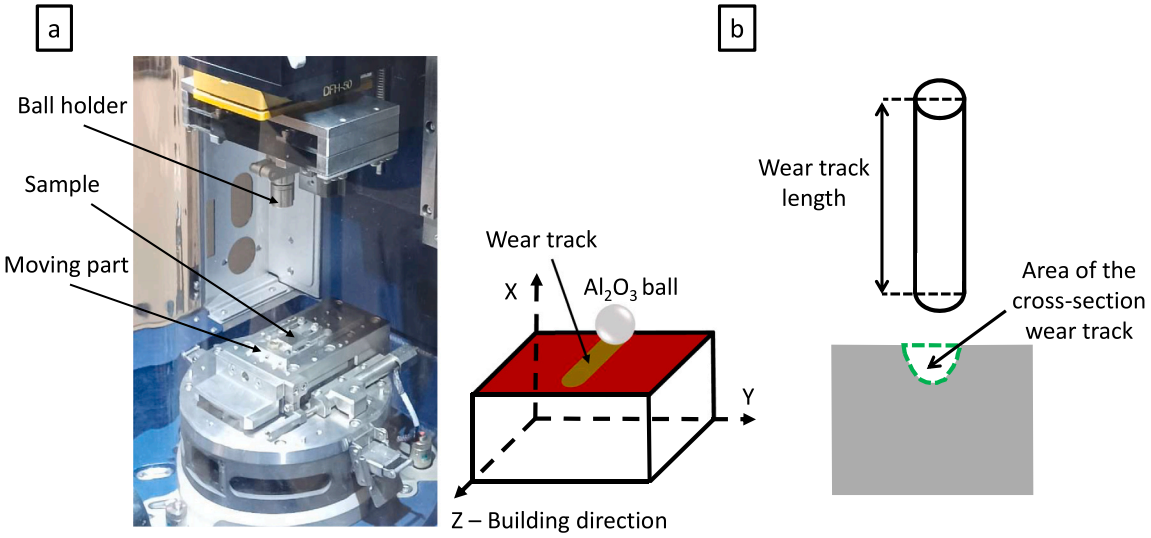

Fig. 2. Illustrations of (a) the experimental device and schematic representation of the tribological test and (b) schemas for measuring the length of the wear track and the area of the wear track cross-section.

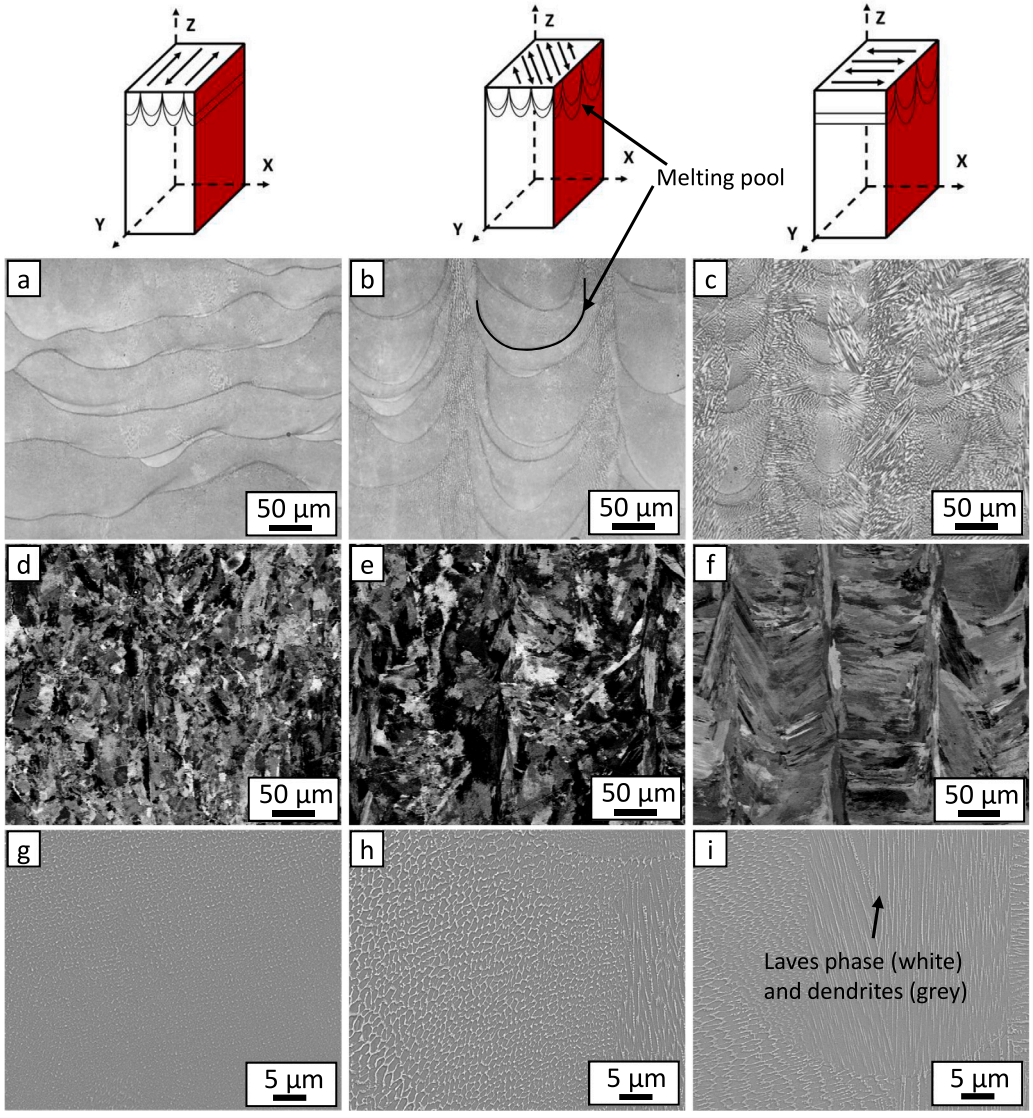

Fig. 3. Microstructure of the parts observed with an optical microscope (a) A0, (b) A45, (c) A90, with SEM-BSE before etching (d) A0, (e) A45 and (f) A90 and with SEM-SE after etching (g) A0, (h) A45 and (i) A90.

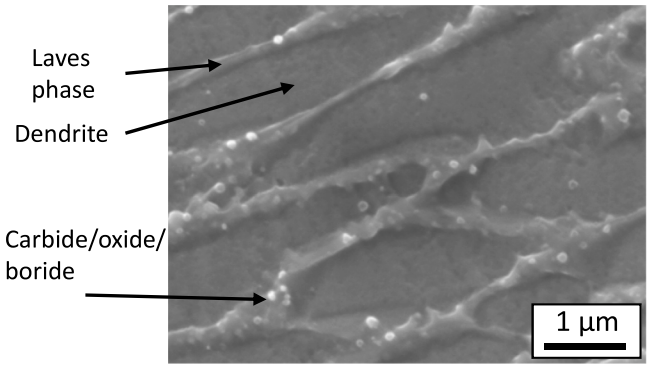

Fig. 4. Microstructure at high magnification of the ABD-900AM part at the as-build state.

shorter than A0 (Fig. 1) implies that A0 and A90 adjacent passes have different heat cycles, which may affect the heat flow and drive the grain growth. For example, for the A0 sample, one laser track lasts 20 µs, against 7 µs for A90. The laser scanning tracks being bidirectional, the time for the laser to return close to the departure point considered in this example and to partially recast the previous track is 40 µs for A0 and 14 µs for A90. However, this phenomenon is not of prime interest to this study because the L-PBF process is used to generate reference microstructures.

In conclusion, the microstructural observations and the phase analysis show that the scanning angle alters the microstructure at different scales, creating morphological and texture anisotropies. The following parts will focus on the correlation between these microstructures and their resulting hardness properties and tribological behaviors.

3.3. Hardness properties and wear tests

3.3.1. Hardness measurements

Hardness tests with a load of 1 kg have been conducted to see if the microstructure difference affects the hardness values. The hardness measured for A0, A45, and A90 are 337 ± 12 HV, 337 ± 7 HV, and 327 ± 7 HV, respectively. The measurements are very close to each other: the microstructure differences do not impact the hardness for this load. The hardness value is related to the atoms in solid solutions (Co, Cr), the carbides in the interdendritic regions, and the fine microstructure induced by the L-PBF process.

3.3.2. Analysis of wear and friction

Fig. 6 shows the wear volume for the different scanning angles and the real-time coefficient of friction of A0-3.

The plate wear volume (Fig. 6a) for A0, A45 and A90 are 0.60 ± 0.12 mm^3, 0.81 ± 0.15 mm^3 and 1.00 ± 0.09 mm^3, respectively. The wear results show a trend between the material removal and the scanning angle. The same trend is observed with the ball wear volume, presented in Fig. 6b. The previous crystallographic texture analysis showed that A0 and A90 exhibit a common $\gamma(200)$ texture (Fig. 5). Moreover, hardness measurements did not permit the dissociation of the different scanning strategies. Thus, the texture approached by phase analysis and the hardness do not permit an explanation of the difference in wear resistance.

The real-time coefficient of friction proposed in Fig. 6c shows three-time phases: P1, P2, and P3. P1 is characterized by a strong amplitude of oscillations that could be related to the emission and circulation of particles in contact. P2 presents an increasing COF with a decrease in the amplitude of macro and micro oscillations. The last phase, P3, shows a reduction and a stabilization of the COF value. The beginning of the decrease of phase P3 is observed for six of the nine tests conducted, and it is believed that with a longer test duration, the reduction and the stabilization might appear for the three remaining tests.

The time of this decrease versus wear volume is reported in Fig. 7. To visualize the wear volume value of every test, the tests for which the decrease did not appear during the tribological tests were set at 3600 s and marked with a cross. The others are labeled with a full circle. For the results marked with a circle, the scanning angle A0 has the shortest times, followed by A45 and A90. The scanning angle impacts the time entrance of P3, but it is hard to conclude its impact on the final wear volume. Noticeably, all the tests marked with a cross have a higher wear value compared to the other tests with the same scanning strategy and marked with a full circle. During the P3 phase, the evolution of wear mechanisms and the emission and circulation of particles in the contact is believed to stabilize.

Fig. 8 shows the real-time coefficient of friction and the real-time penetration depth of the ball holder for the three scanning angles. The real-time coefficients of friction show that A0 is the more perturbed in the P1 phase, with high time fluctuation in the P2 phase. Fluctuations are also detectable for A45 and A90 in the P2 phase but with higher frequency. The real-time penetration depth of the ball for the three scanning angles, presented in Fig. 8d, also shows different trends. P1 shows high wear, and instabilities are detectable between the beginning of the test and 1000 s following the scanning angle: A0 is the part that has the most instabilities, followed by A45 and A90. The instabilities on the coefficient of friction, the penetration of the ball holder, and the high time fluctuations are linked to the ability of the parts to form their debris and the repeatability of the mechanisms.

After the tests, samples were observed with an SEM-BSE to quantify by image analysis the percentage of oxide layers on the surface of the wear tracks. The acquisition was made at the middle of the stroke length and took all the wear track's width, as shown in Fig. 9.

It is a simple approach to highlight a trend, but it does not consider the different characteristics of the oxides: their nature, oxygen concentration, dispersion, and size. The percentage of oxide layers on the surface decreases with the increase of the scanning angle. The percentage of oxide layers on the surface for A0, A45 and A90 are 35 ± 8%, 31 ± 5% and 25 ± 5%, respectively. It is related to the scanning angle and the wear volume. The oxides formed on the wear track had a lubricant effect and reduced the wear of the samples. The high amount of oxide layers reduces the metal/ceramic contact. Fig. 10 shows the percentage of oxide layers on the surface for each test. A strong trend exists between the scanning strategy, the percentage of oxide layers on the surface, and the wear volume. However, there is no clear link between the beginning of the P3 phase and the amount of oxide layers on the surface.

3.3.3. Characterization of worn surface

The analysis of the wear tracks of L-PBF parts characterized by the SEM focused on identifying and interpreting wear mechanisms detected for each sample. For every wear test, observations were made in the center, the edges, and at the end of the wear tracks. To avoid confusion, the terms particles and debris are defined as follows. A particle is matter made up of one or more antagonists, with or without reaction with the environment, and which has not been definitively ejected from the wear track. Debris, or wear debris, has the same definition as a particle from a material point of view, but has been definitively ejected from the wear track.

The worn surface of the two first bodies was investigated at different scales: with an optical microscope to observe the wear particles right after the tests for both antagonists and with an SEM for the L-PBF parts to assess the wear mechanisms. The worn surfaces after the wear tests are shown in Fig. 11. On the L-PBF parts, the particles detached from the two first bodies are mainly ejected at the end of the wear track and on the edges. However, A0 particles demonstrate more freedom of mobility. On the contrary, A45 and A90 particles are trapped at the end of the wear track. This phenomenon is due to the particle's aggregation,

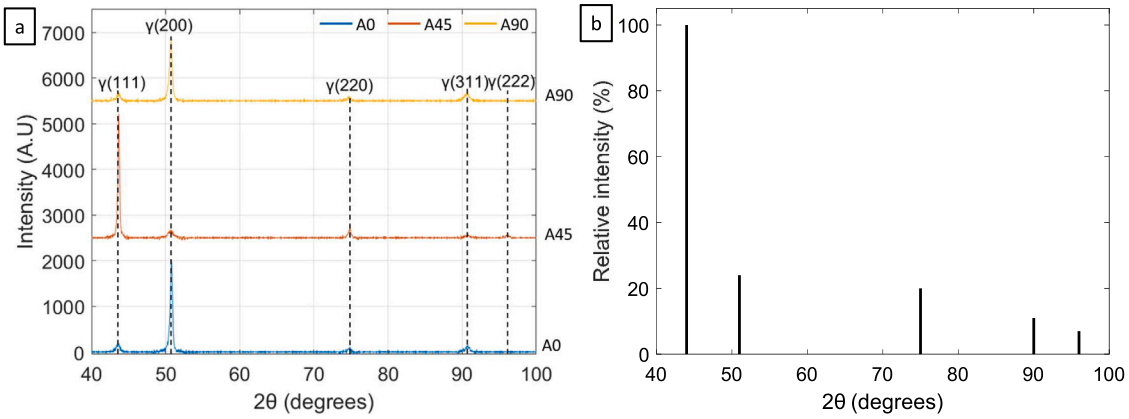

Fig. 5. (a) Phase analysis of the ABD-900AM parts for A0, A45, and A90 and (b) theoretical diffractogram for a non-textured CFC material.

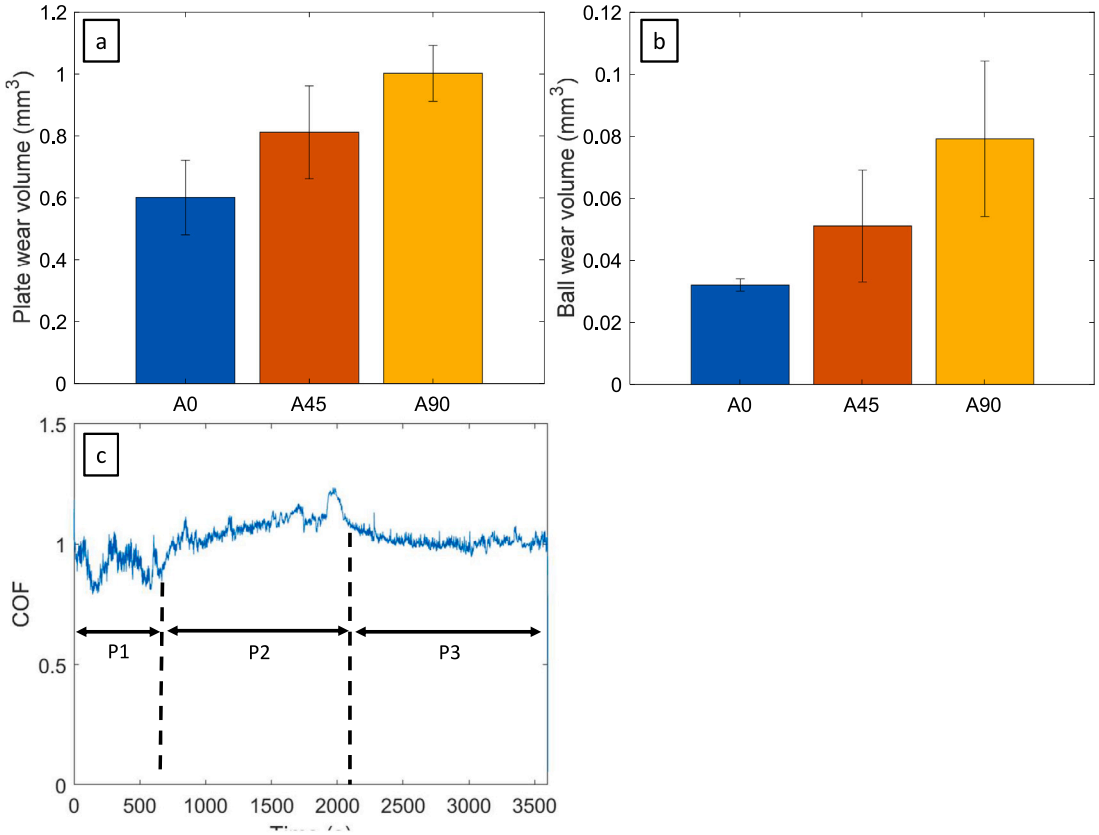

Fig. 6. Wear and friction results from tribological tests. (a) Wear volume of ABD-900AM parts, (b) ball wear volume and (c) real-time coefficient of friction of A0-3.

which is more significant for A45 and A90 than A0. Due to different oxidation, the particles at the end of the wear track are darker than the particles on the edges. The particles were mainly ejected out of the track during the wear tests. Only some patches of oxides are seen in the wear track. The balls present black adherent particles that are oxidized metallic particles.

Fig. 12 shows a part of the bottom of the wear track. The L-PBF part presents material plastic flow and shear bands out of the wear track due to the high pressure induced by the contact and the ability of the material to accommodate the load. The presence of shear bands ensures that the displacement of dislocations is possible over large distances and contributes to the accommodation of plastic deformation. The BSE detector highlights black particles in the wear track (Fig. 12a,c). EDS analysis made on one of these particles, exposed in Table 5, showed that these are alumina particles embedded in the wear track. The quantity of these alumina particles implies that they come from the alumina ball, not the alumina present at the as-fabricated state. A higher magnification of the view of the wear track (Fig. 12b) shows cupules, a sign of the ductile rupture of a particle due to tensile and shear stresses. The cupules are only observed at the top and bottom of the wear tracks. Fig. 12d shows the ball wear track. The surface exhibits transferred layers composed of particles that have been compacted in the contact. The wear track also shows the granular structure of the alumina ball. Micrometer-sized grains are composed of facets with sharp edges and can act as abrasive asperities, similar to a rapier. The ball is damaged through grain detachment, contributing to the formation of the third body.

The side track in Fig. 13 shows a particle of 50 μm width and 120 μm length detached from the wear track. This type of particle is expected

Table 5
Identification of a particle embedded in the wear track by chemical analysis.

Elements	O	Al	Ti	Cr	Co	Ni	Nb	Mo	W
Spectrum 1 (% at.)	58.08	35.18	0.26	1.76	1.51	3.22	–	–	–
Spectrum 2 (% at.)	35.35	3.84	1.75	12.47	12.81	31.42	0.7	0.87	0.79

Table 6
Chemical analysis of the oxide layers observed on the wear tracks Fig. 15.

Elements	O	Ni	Co	Cr	Al	Ti	Nb	Mo	Ta	W
Fig. 15a (% at.)	58.36	21.32	8.2	7.19	2.27	1.06	0.45	0.47	0.22	0.46
Fig. 15b (% at.)	38.11	31.85	12.26	10.73	3.24	1.57	0.58	0.66	0.32	0.69

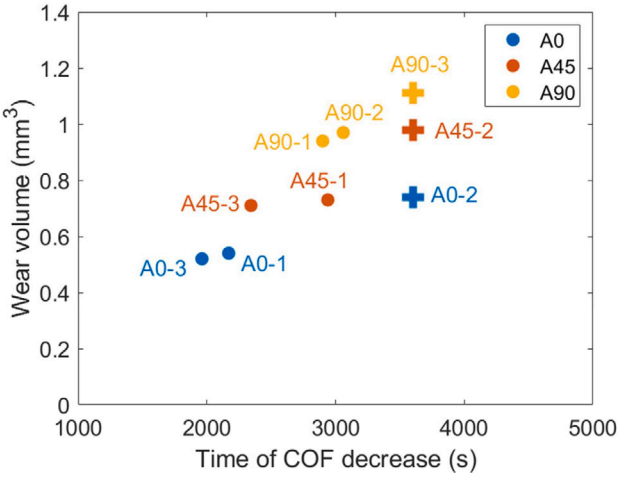

Fig. 7. Wear volume as a function of each test's time of COF decrease. The tests without P3 are set at 3600 s and marked with a cross.

to be the particles observed after the wear test on the sides of the wear track with a gray color. The particle's surface is partially oxidized, meaning that these particle circulated in the contact.

The characterization of the wear track center in Fig. 14 shows grooves parallel to the sliding direction, a sign of abrasive wear. The ductile behavior of the material implies that the grooves made by a harder particle, such as oxidized particles or alumina, lead to plastic deformation of the surface but not necessarily to the formation of a particle. The oxides present in the wear track are either in patches or elongated along the sliding direction. Cavities with sizes ranging from submicronic to a few micrometers were observed on the surface, as shown in Fig. 14b. The picture at higher magnification indicates that the biggest cavities are filled with particles, so they did not appear at the end of the test but occurred during sliding. These cavities show a lack of cohesion at the extreme surface and may be formed due to the accumulation of plastic strain.

The oxides observed in the wear track, mainly at the top and the bottom, do not have a constant chemical composition, as seen in Fig. 15 with the SEM-BSE images and chemical analysis which is shown Table 6. This difference in oxygen content may also be due to the oxide layer thickness.

The first type of oxide detected (Fig. 15a) has the highest oxygen content. The surface of the oxide is composed of a smooth layer with various cracks. Some cracks are wavy, while others are sharper and straighter. The image of a straight crack at higher magnification (top right corner of Fig. 15a) shows that the edges of the crack are sharp and that no debris is trapped inside. This kind of crack occurs at the end of the test due to the difference in the coefficient of thermal expansion. The wavy crack forms come from the ball's motion on the plate. The ball-induced stresses are compressive in the front of the contact and tensile at the back of the ball. The oxides have a brittle behavior, which explains the formation of these cracks. The other kind of oxide detected on the surface (Fig. 15b) had lower oxygen content, probably due to its thickness. A smoother surface and fewer cracks characterize it. The lower amount of oxygen in this layer may reduce its fragile behavior and thus explain why fewer cracks are detectable. Both layers are composed of small oxidized metallic particles with a spherical shape that are aggregated, compacted, and laminated under the pressure induced by the ball. The smooth texture shows their load-bearing capacity concerning the zones composed of spherical particles. The particles' size and spherical morphology suggest that these particles circulated in the contact. The oxides detected imply that oxidative wear occurs.

3.3.4. Wear debris

The wear debris of each scanning angle was investigated with the SEM. The examination of the wear debris focused on the nature of the debris observed.

Fig. 16 shows that wear debris can be classified into two types: oxidized debris in gray and non-oxidized debris in white. Debris are mainly composed of oxidized debris with a plate-like morphology. An acquisition at a higher magnification of the wear debris is shown in Fig. 17. The first type of oxidized debris (Fig. 17a) has a plate-like morphology. It comprises submicronic metallic debris that have been oxidized, agglomerated and compacted in the contact with a thickness of a few micrometers. The limited thickness observed shows that the agglomerated particles tend to have critical thicknesses before ejection from the contact. The wear oxidized debris observed for the different scanning angles have the same features: an accumulation of debris with a smooth or rough surface. The oxides in Fig. 15a were observed only once out of all the debris observations, shown in Fig. 17c. The debris did not have straight cracks formed at the end of the test. This implies that the ejection of these oxides out of the wear track is limited. Once they are spalled off, they must be fragmented into smaller particles. It is confirmed that the black debris observed with the numerical microscope in Fig. 11c is oxidized debris. The other type of debris (Fig. 17b) differs in its morphology, which looks like an agglomeration of smaller debris. Its shape lets us suppose that these debris have been created by accumulating smaller particles stocked together and pushed out by the ball. The debris detached from the wear track have a plate-like morphology (Fig. 17d) and correspond to the white debris Fig. 16. The surface shows abrasion marks and plastic deformation and contains embedded alumina particles. Alumina particles are not coherent with the surrounding material because the crack tends to go around the alumina particles (Fig. 17e).

3.3.5. Cross-section worn surface

The SEM technique was used to characterize the cross-section worn surface. The pictures in Fig. 18 show the typical features observed from the cross-section of each scanning angle. A plastic flow of almost 10 micrometers under the worn surface is observable. This plastic flow is viewable thanks to the load-induced deformation of the cells and the surrounding Laves phase.

The ball motion imposes the plastic flow and is expected to be along the same vector. Fig. 18a highlights a plastic flow in the same direction as the last ball motion; however, Fig. 18b also presents a

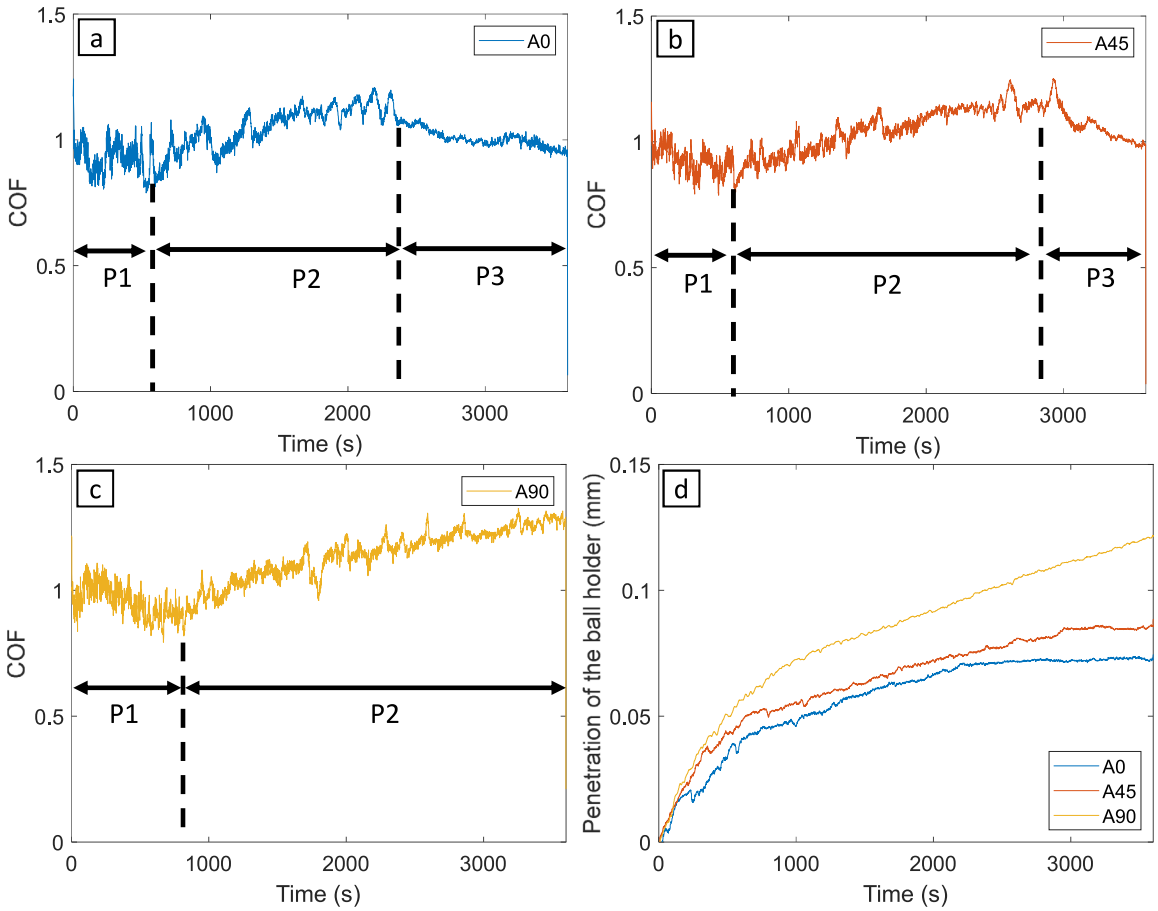

Fig. 8. Real-time coefficient of friction of (a) A0, (b) A45, (c) A90, and (d) penetration depth of the ball for the three scanning angles.

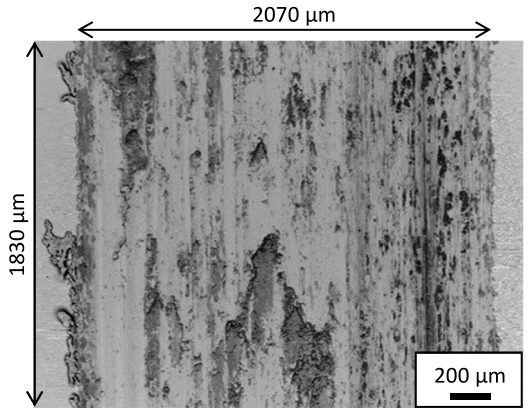

Fig. 9. SEM-BSE image of the wear track's center.

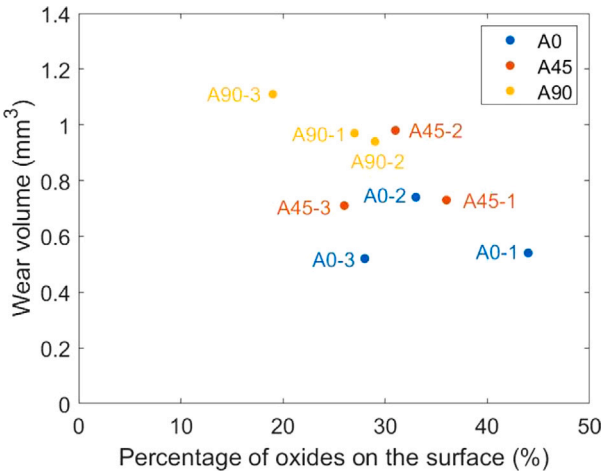

Fig. 10. Influence of the scanning angle on the wear volume of each test according to its percentage of oxide layers on the surface.

plastic flow in the opposite direction. This may be due to a protective layer accommodating all the load and velocity or because the surface of the deformed layer was not in contact with the ball during its last motion. Fig. 18a presents an oxide layer with a crack perpendicular to the sliding, which leads to a pore and is free of particles. This crack is believed to be one of the cracks observed on the worn surface Fig. 15. Another crack parallel to the worn surface is also visible. It shows the delamination of a particle one micrometer thick. Fig. 18b shows a layer, where the Laves phase is almost totally dissolved. This deformed layer is not present in all the lengths of the wear track, and its thickness ranges from less than a micrometer to 4 µm. The same pores are observed in 18a and Fig. 18b. The lack of pores inside the bulk and under the friction surface implies that these pores were formed due to the wear tests. Slip bands are detectable under the friction surface (Fig. 18c) down to almost 10 µm and with an angle of ±45° with the friction surface.

At the top of the deformed layer Fig. 18b,c a hollow indicated by a yellow arrow shows a particle detached from this layer. These layers, therefore, appear to be a source of particle production. The repeated motions of the ball over this layer incrementally increase the

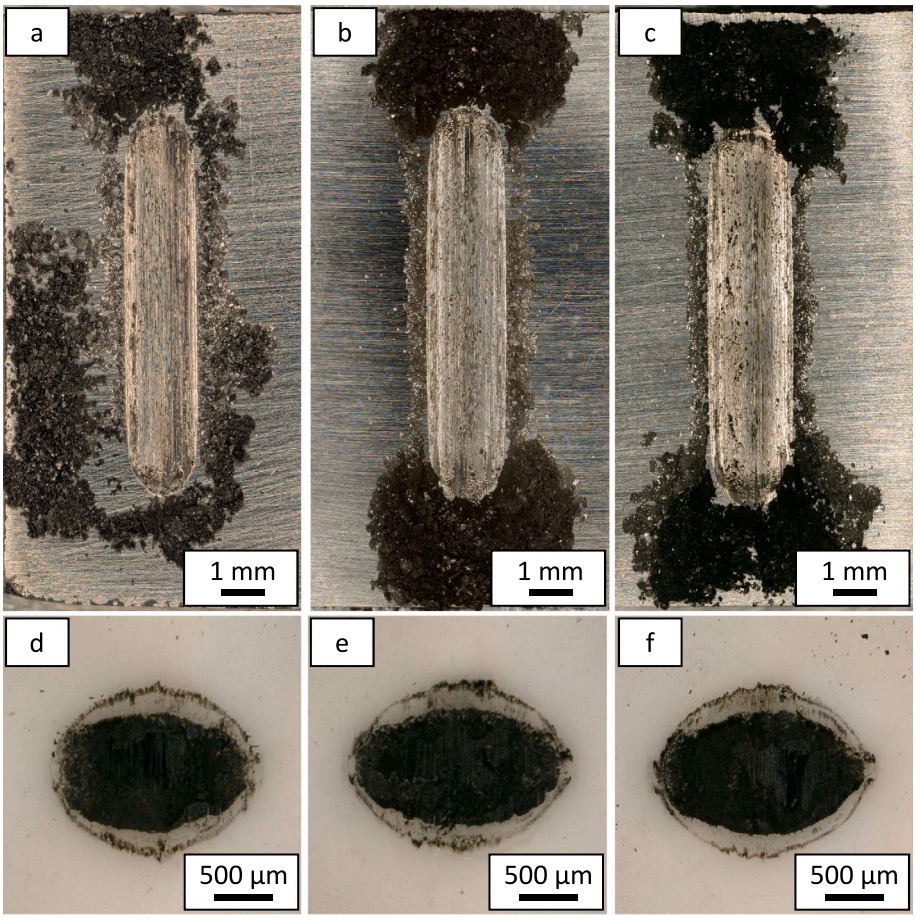

Fig. 11. Worn surface of the plate (a–c) and the ball (d–f) before cleaning for (a),(d) A0, (b),(e) A45 and (c),(f) A90.

plastic strain of the layer, which eventually reaches a local critical strain rate that leads to the formation and propagation of a crack parallel to the sliding direction and finally to the delamination of a particle [35]. Other researchers who worked on 316L and Inconel 718, showed that the main deformation mechanism in L-PBF parts is governed by dislocation motion, whose movement is blocked by the dislocation network present in the as-built state [36,37]. The particle is then emitted into the wear track and is either ejected permanently from the wear track or laminated and fragmented by the repeated motions of the ball. Cross-sectional observations suggest that the abovementioned process mainly governs particle emission from the superalloy plates. Establishing an oxidized layer on the deformed layer would protect it and reduce wear on the part, as it has been observed by Zurcher et al. [38] on Inconel 718 manufactured with the Laser Metal Deposition process. Thus, the difference in wear resistance according to the scanning strategy could be linked to the oxide layers on the plate's wear track. The morphology of the cells and the homogeneity of the cellular structure may also contribute to maintain this protective layer on the wear track by the strengthening it brings to the matrix. Thus, the homogeneous equiaxed cellular structure of the A0 strategy results in the lowest wear, followed by the A45 strategy, which has a similar morphology but a coarser cellular structure between its melt pools. Finally, the A90 strategy features a cellular structure that is also coarser between its melt pools, but with a columnar structure. This size heterogeneity within the melt pools leads to reduced wear resistance, and the columnar cell morphology appears to be more detrimental than an equiaxed morphology, which explains the wear difference between A45 and A90.

4. Conclusion

This study explores the wear behavior of parts built with a specific building strategy, focusing on the real-time coefficient of friction and the identification of wear mechanisms. The main conclusions are reported as follows:

1. The ABD-900AM microstructure obtained with the L-PBF process for three scanning angles (0°, 45°, and 90°) consists of a dense material with grain structure evolution from equiaxed to columnar. The crystallographic texture is related to the scanning angle, with a texture of $\gamma(200)$, $\gamma(111)$ and $\gamma(200)$ for A0, A45 and A90, respectively.
2. The plate wear volume for A0, A45 and A90 are 0.60 ± 0.12 mm^3, 0.81 ± 0.15 mm^3 and 1.00 ± 0.09 mm^3, respectively. The wear volume strongly depends on the scanning angle and is related to the percentage of the oxide layers on the surface. The strengthening brought by the homogeneity in the cellular structure contributes to maintain the oxide layers.
3. The real-time coefficient of friction shows three distinct phases associated with an evolution of wear mechanisms during the sliding test. All the parts were worn according to the same wear mechanism, the abrasion.

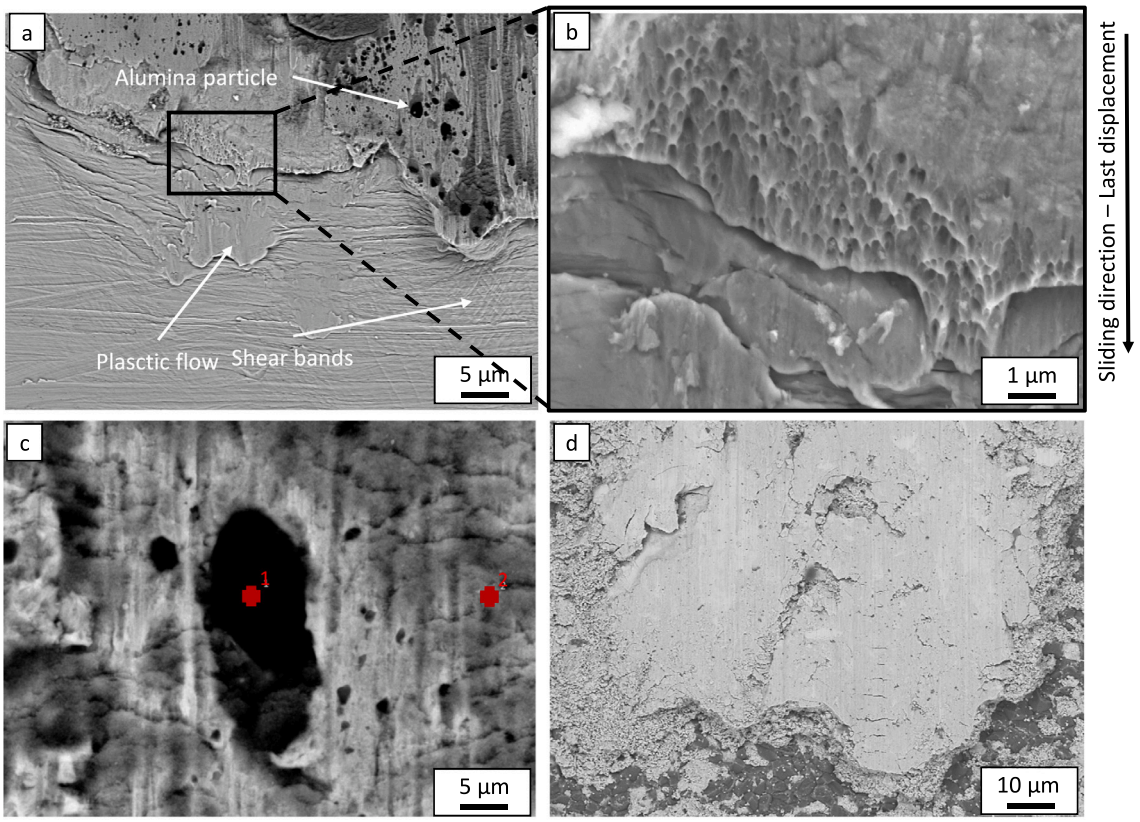

Fig. 12. SEM observations of the bottom of the wear track. (a) BSE imaging, (b) SE image at higher magnification of the cupules, (c) particle embedded in the wear track and (d) ball wear track observed with BSE.

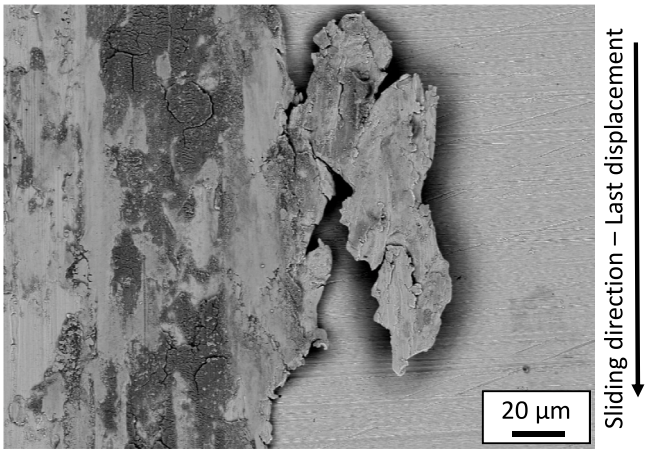

Fig. 13. SEM-BSE observation of a particle detaching from the edge of the wear track.

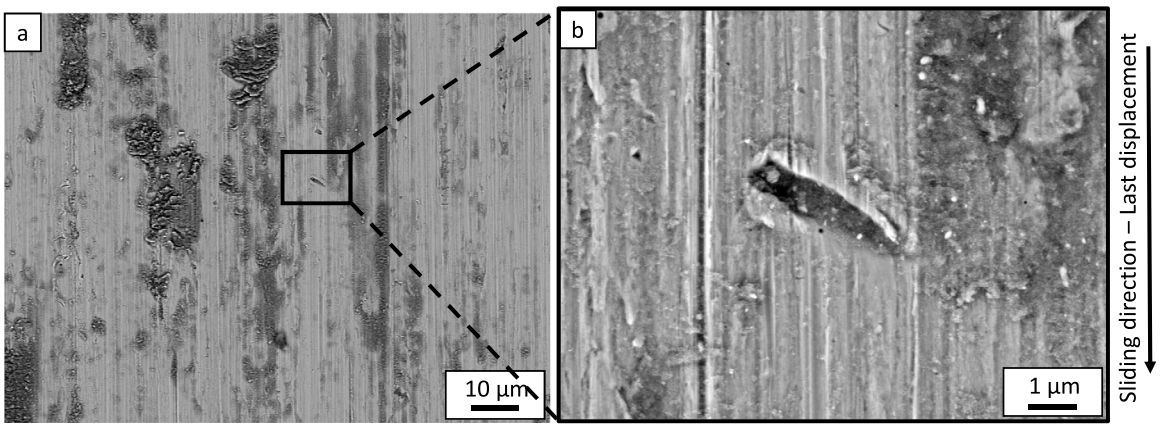

Fig. 14. SEM-BSE observation of the wear track center at (a) low magnification and (b) high magnification.

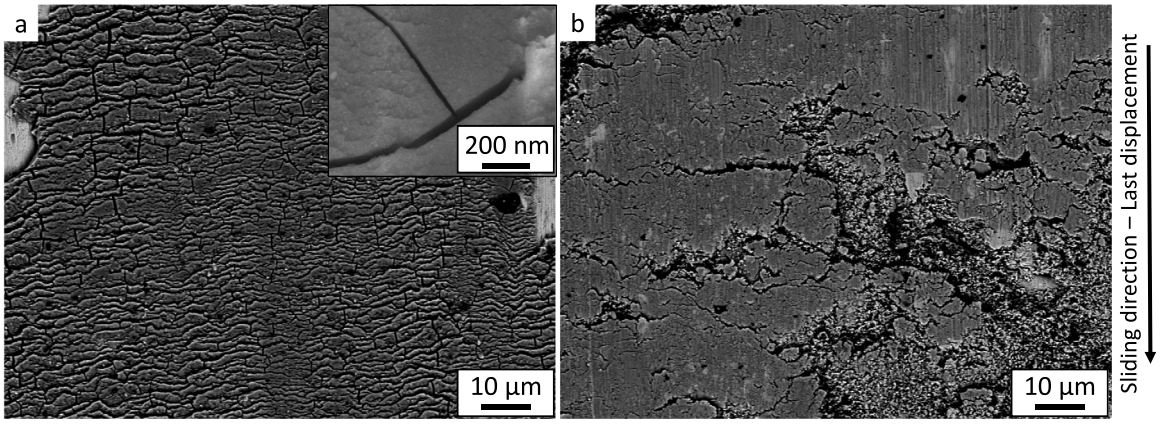

Fig. 15. SEM-BSE observation of oxides in the wear track. (a) and (b) two layers of oxides.

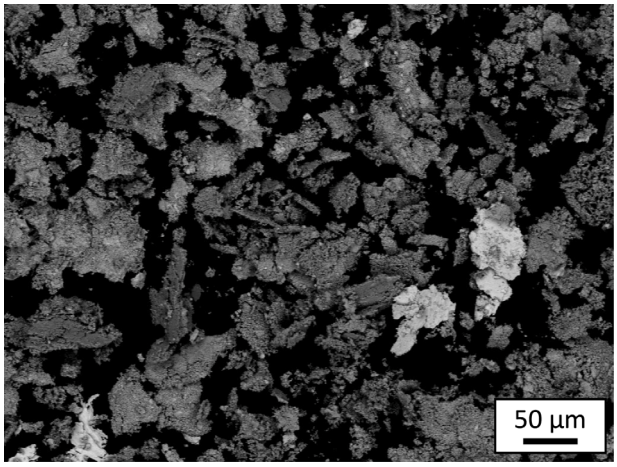

Fig. 16. SEM-BSE observation of the wear debris.

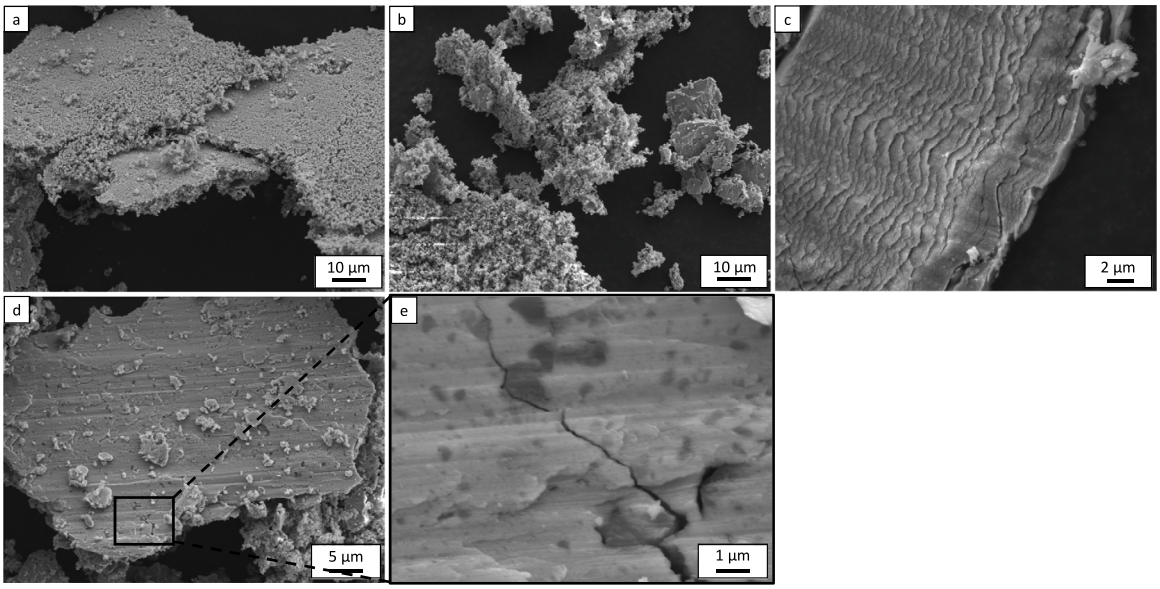

Fig. 17. SEM observation of (a),(b),(c) oxidized spherical debris agglomerated (d),(e) plate-like debris detached from the plate.

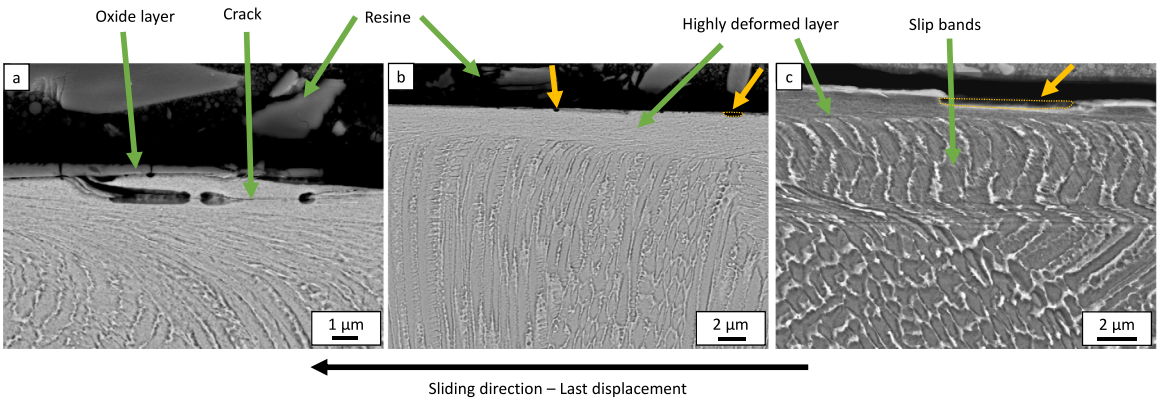

Fig. 18. SEM observations of the cross-section worn surface. (For interpretation of the references to color in this figure legend, the reader is referred to the web version of this article.)

CRediT authorship contribution statement

Pierre-Nicolas Parent: Writing – original draft. **Jean-Yves Paris:** Writing – review & editing, Conceptualization. **Joël Alexis:** Writing – review & editing, Conceptualization. **Christine Boher:** Writing – review & editing, Conceptualization.

Declaration of competing interest

The authors declare that they have no known competing financial interests or personal relationships that could have appeared to influence the work reported in this paper.

Data availability

Data will be made available on request.

References

[1] T.M. Pollock, S. Tin, Nickel-based superalloys for advanced turbine engines: Chemistry, microstructure and properties, J. Propuls. Power 22 (2) (2006) 361–374, http://dx.doi.org/10.2514/1.18239, URL https://arc.aiaa.org/doi/10.2514/1.18239.

[2] R. Smith, G. Lewi, D. Yates, Development and application of nickel alloys in aerospace engineering, Aircr. Eng. Aerosp. Technol. 73 (2) (2001) 138–147, http://dx.doi.org/10.1108/00022660110694995, Publisher: MCB UP Ltd.

[3] R.C. Reed, The Superalloys: Fundamentals and Applications, Cambridge University Press, Cambridge, 2006, http://dx.doi.org/10.1017/CBO9780511541285, URL https://www.cambridge.org/core/books/superalloys/00CEE7E1026FA82BBC9F335E75D57AB2.

[4] M.J. Donachie, S.J. Donachie, Superalloys: A Technical Guide, second ed., ASM International, Materials Park, OH, 2002.

[5] S. Sanchez, P. Smith, Z. Xu, G. Gaspard, C.J. Hyde, W.W. Wits, I.A. Ashcroft, H. Chen, A.T. Clare, Powder bed fusion of nickel-based superalloys: A review, Int. J. Mach. Tools Manuf. 165 (2021) 103729, http://dx.doi.org/10.1016/j.ijmachtools.2021.103729, URL https://www.sciencedirect.com/science/article/pii/S0890695521000390.

[6] G.H. Gessinger, Powder metallurgy of superalloys, Butterworths monographs in materials, Butterworths, London ; Boston, 1984.

[7] M.C. Lam, S.C.V. Lim, H. Song, Y. Zhu, X. Wu, A. Huang, Scanning strategy induced cracking and anisotropic weakening in grain texture of additively manufactured superalloys, Addit. Manuf. (2022) 102660, http://dx.doi.org/10.1016/j.addma.2022.102660, URL https://www.sciencedirect.com/science/article/pii/S2214860422000665.

[8] D. Grange, J. Bartout, B. Macquaire, C. Colin, Processing a non-weldable nickel-base superalloy by selective laser melting: role of the shape and size of the melt pools on solidification cracking, Materialia 12 (2020) 100686, http://dx.doi.org/10.1016/j.mtla.2020.100686, URL https://linkinghub.elsevier.com/retrieve/pii/S2589152920301034.

[9] Y. Zhou, X. Li, C. Guo, X. Hu, Q. Zhu, Investigation of columnar to equiaxial transition criterion and solidification conditions for Ni-based superalloy in laser powder bed fusion, J. Alloys Compd. 966 (2023) 171611, http://dx.doi.org/10.

1016/j.jallcom.2023.171611, URL https://linkinghub.elsevier.com/retrieve/pii/S0925838823029146.
[10] J.N. Ghoussoub, Y.T. Tang, C. Panwisawas, A. Németh, R.C. Reed, On the influence of alloy chemistry and processing conditions on additive manufacturability of Ni-based superalloys, in: S. Tin, M. Hardy, J. Clews, J. Cormier, Q. Feng, J. Marcin, C. O'Brien, A. Suzuki (Eds.), Superalloys 2020, in: The Minerals, Metals & Materials Series, Springer International Publishing, Cham, 2020, pp. 153–162, http://dx.doi.org/10.1007/978-3-030-51834-9_15.
[11] J.N. Ghoussoub, Y.T. Tang, W.J.B. Dick-Cleland, A.A.N. Németh, Y. Gong, D.G. McCartney, A.C.F. Cocks, R.C. Reed, On the influence of alloy composition on the additive manufacturability of Ni-based superalloys, Metall. Mater. Trans. A 53 (3) (2022) 962–983, http://dx.doi.org/10.1007/s11661-021-06568-z, URL https://link.springer.com/10.1007/s11661-021-06568-z.
[12] Y.T. Tang, C. Panwisawas, J.N. Ghoussoub, Y. Gong, J.W. Clark, A.A. Németh, D.G. McCartney, R.C. Reed, Alloys-by-design: Application to new superalloys for additive manufacturing, Acta Mater. 202 (2021) 417–436, http://dx.doi.org/10.1016/j.actamat.2020.09.023, URL https://linkinghub.elsevier.com/retrieve/pii/S1359645420307175.
[13] A. Hussein, L. Hao, C. Yan, R. Everson, Finite element simulation of the temperature and stress fields in single layers built without-support in selective laser melting, Mater. Des. (1980-2015) 52 (2013) 638–647, http://dx.doi.org/10.1016/j.matdes.2013.05.070, URL https://linkinghub.elsevier.com/retrieve/pii/S0261306913005025.
[14] S. Cooke, K. Ahmadi, S. Willerth, R. Herring, Metal additive manufacturing: Technology, metallurgy and modelling, J. Manuf. Process. 57 (2020) 978–1003, http://dx.doi.org/10.1016/j.jmapro.2020.07.025, URL https://www.sciencedirect.com/science/article/pii/S1526612520304503.
[15] O. Gokcekaya, T. Ishimoto, S. Hibino, J. Yasutomi, T. Narushima, T. Nakano, Unique crystallographic texture formation in inconel 718 by laser powder bed fusion and its effect on mechanical anisotropy, Acta Mater. 212 (2021) 116876, http://dx.doi.org/10.1016/j.actamat.2021.116876, URL https://www.sciencedirect.com/science/article/pii/S1359645421002561.
[16] P. Tao, H. Li, B. Huang, Q. Hu, S. Gong, Q. Xu, The crystal growth, intercellular spacing and microsegregation of selective laser melted inconel 718 superalloy, Vacuum 159 (2019) 382–390, http://dx.doi.org/10.1016/j.vacuum.2018.10.074, URL https://linkinghub.elsevier.com/retrieve/pii/S0042207X18319845.
[17] Q. Zhong, K. Wei, T. Ouyang, X. Li, X. Zeng, Effect of rotation angle on surface morphology, microstructure, and mechanical properties of inconel 718 alloy fabricated by high power laser powder bed fusion, J. Mater. Sci. Technol. 154 (2023) 30–42, http://dx.doi.org/10.1016/j.jmst.2023.01.021, URL https://linkinghub.elsevier.com/retrieve/pii/S1005030223001998.
[18] H. Wan, Z. Zhou, C. Li, G. Chen, G. Zhang, Effect of scanning strategy on mechanical properties of selective laser melted inconel 718, Mater. Sci. Eng. A 753 (2019) 42–48, http://dx.doi.org/10.1016/j.msea.2019.03.007, URL https://linkinghub.elsevier.com/retrieve/pii/S0921509319302989.
[19] V. Popovich, E. Borisov, A. Popovich, V. Sufiiarov, D. Masaylo, L. Alzina, Functionally graded inconel 718 processed by additive manufacturing: Crystallographic texture, anisotropy of microstructure and mechanical properties, Mater. Des. 114 (2017) 441–449, http://dx.doi.org/10.1016/j.matdes.2016.10.075, URL https://linkinghub.elsevier.com/retrieve/pii/S026412751631382X.
[20] S.-H. Sun, K. Hagihara, T. Nakano, Effect of scanning strategy on texture formation in Ni-25at.%mo alloys fabricated by selective laser melting, Mater. Des. 140 (2018) 307–316, http://dx.doi.org/10.1016/j.matdes.2017.11.060, URL https://www.sciencedirect.com/science/article/pii/S0264127517310900.
[21] X. Liu, K. Wang, P. Hu, X. He, B. Yan, X. Zhao, Formability, microstructure and properties of inconel 718 superalloy fabricated by selective laser melting additive manufacture technology, Materials 14 (4) (2021) 991, http://dx.doi.org/10.3390/ma14040991, URL https://www.mdpi.com/1996-1944/14/4/991.
[22] Q. Jia, D. Gu, Selective laser melting additive manufactured inconel 718 superalloy parts: High-temperature oxidation property and its mechanisms, Opt. Laser Technol. 62 (2014) 161–171, http://dx.doi.org/10.1016/j.optlastec.2014.03.008, URL https://www.sciencedirect.com/science/article/pii/S0030399214000632.
[23] X. Yan, S. Gao, C. Chang, J. Huang, K. Khanlari, D. Dong, W. Ma, N. Fenineche, H. Liao, M. Liu, Effect of building directions on the surface roughness, microstructure, and tribological properties of selective laser melted inconel 625, J. Mater. Process. Technol. 288 (2021) 116878, http://dx.doi.org/10.1016/j.jmatprotec.2020.116878, URL https://linkinghub.elsevier.com/retrieve/pii/S0924013620302922.
[24] H. Li, M. Ramezani, M. Li, C. Ma, J. Wang, Tribological performance of selective laser melted 316l stainless steel, Tribol. Int. 128 (2018) 121–129, http://dx.doi.org/10.1016/j.triboint.2018.07.021, URL https://linkinghub.elsevier.com/retrieve/pii/S0301679X18303499.
[25] M. Bahshwan, C.W. Myant, T. Reddyhoff, M.-S. Pham, The role of microstructure on wear mechanisms and anisotropy of additively manufactured 316l stainless steel in dry sliding, Mater. Des. 196 (2020) 109076, http://dx.doi.org/10.1016/j.matdes.2020.109076, URL https://linkinghub.elsevier.com/retrieve/pii/S0264127520306110.
[26] A. Spierings, M. Schneider, R. Eggenberger, Comparison of density measurement techniques for additive manufactured metallic parts, Rapid Prototyp. J. 17 (5) (2011) 380–386, http://dx.doi.org/10.1108/13552541111156504, URL https://www.emerald.com/insight/content/doi/10.1108/13552541111156504/full/html.
[27] S. Kucharski, Z. Mróz, Identification of wear process parameters in reciprocating ball-on-disc tests, Tribol. Int. 44 (2) (2011) 154–164, http://dx.doi.org/10.1016/j.triboint.2010.10.010, URL https://www.sciencedirect.com/science/article/pii/S0301679X10002537.
[28] A.T. Pérez, A.H. Battez, G. García-Atance, J.L. Viesca, R. González, M. Hadfield, Use of optical profilometry in the ASTM d4172 standard, Wear 271 (11) (2011) 2963–2967, http://dx.doi.org/10.1016/j.wear.2011.06.016, URL https://www.sciencedirect.com/science/article/pii/S004316481100456X.
[29] M. Beltowksi, P.J. Blau, J. Qu, Wear of spheroidal graphite cast irons for tractor drive train components, Wear 267 (9) (2009) 1752–1756, http://dx.doi.org/10.1016/j.wear.2009.03.030, URL https://www.sciencedirect.com/science/article/pii/S0043164809002956.
[30] E.P. Whitenton, P.J. Blau, A comparison of methods for determining wear volumes and surface parameters of spherically tipped sliders, Wear 124 (3) (1988) 291–309, http://dx.doi.org/10.1016/0043-1648(88)90219-0, URL https://www.sciencedirect.com/science/article/pii/0043164888902190.
[31] Y.T. Tang, C. Panwisawas, B.M. Jenkins, J. Liu, Z. Shen, E. Salvati, Y. Gong, J.N. Ghoussoub, S. Michalik, B. Roebuck, P.A.J. Bagot, S. Lozano-Perez, C.R.M. Grovenor, M.P. Moody, A.M. Korsunsky, D.M. Collins, R.C. Reed, Multi-length-scale study on the heat treatment response to supersaturated nickel-based superalloys: Precipitation reactions and incipient recrystallisation, Addit. Manuf. (2023) 103389, http://dx.doi.org/10.1016/j.addma.2023.103389, URL https://www.sciencedirect.com/science/article/pii/S2214860423000027.
[32] K. Amato, S. Gaytan, L. Murr, E. Martinez, P. Shindo, J. Hernandez, S. Collins, F. Medina, Microstructures and mechanical behavior of inconel 718 fabricated by selective laser melting, Acta Mater. 60 (5) (2012) 2229–2239, http://dx.doi.org/10.1016/j.actamat.2011.12.032, URL https://linkinghub.elsevier.com/retrieve/pii/S1359645411008949.
[33] J. Xu, Y. Ding, Y. Gao, H. Wang, Y. Hu, D. Zhang, Grain refinement and crack inhibition of hard-to-weld inconel 738 alloy by altering the scanning strategy during selective laser melting, Mater. Des. 209 (2021) 109940, http://dx.doi.org/10.1016/j.matdes.2021.109940, URL https://www.sciencedirect.com/science/article/pii/S0264127521004949.
[34] H.Y. Wan, Z.J. Zhou, C.P. Li, G.F. Chen, G.P. Zhang, Effect of scanning strategy on grain structure and crystallographic texture of inconel 718 processed by selective laser melting, J. Mater. Sci. Technol. 34 (10) (2018) 1799–1804, http://dx.doi.org/10.1016/j.jmst.2018.02.002, URL https://www.sciencedirect.com/science/article/pii/S1005030218300252.
[35] C. Boher, O. Barrau, R. Gras, F. Rezai-Aria, A wear model based on cumulative cyclic plastic straining, 17th International Conference on Wear of Materials, Wear 267 (5) (2009) 1087–1094, http://dx.doi.org/10.1016/j.wear.2009.01.010, URL https://www.sciencedirect.com/science/article/pii/S0043164809000532.
[36] X. Liu, R. Hu, C. Yang, X. Luo, Y. Hou, J. Bai, R. Ma, Strengthening mechanism of a Ni-based superalloy prepared by laser powder bed fusion: The role of cellular structure, Mater. Des. 235 (2023) 112396, http://dx.doi.org/10.1016/j.matdes.2023.112396, URL https://linkinghub.elsevier.com/retrieve/pii/S0264127523008110.
[37] L. Liu, Q. Ding, Y. Zhong, J. Zou, J. Wu, Y.-L. Chiu, J. Li, Z. Zhang, Q. Yu, Z. Shen, Dislocation network in additive manufactured steel breaks strength–ductility trade-off, Mater. Today 21 (4) (2018) 354–361, http://dx.doi.org/10.1016/j.mattod.2017.11.004, URL https://linkinghub.elsevier.com/retrieve/pii/S1369702117304625.
[38] T. Zurcher, G. Bouvard, J.-C. Abry, E. Charkaluk, V. Fridrici, Effect of the scanning strategy and tribological conditions on the wear resistance of IN718 obtained by laser metal deposition, Wear 534–535 (2023) 205152, http://dx.doi.org/10.1016/j.wear.2023.205152, URL https://linkinghub.elsevier.com/retrieve/pii/S0043164823005355.